Nonlinear-mode-coupling-induced soliton crystal dynamics in optical microresonators

Tianye Huang,[1,2,*] Jianxing Pan,[1] Zhuo Cheng,[1] Gang Xu,[3] Zhichao Wu,[1] Taoyuan Du,[4] Shuwen Zeng,[5] and Perry Ping Shum[1]

[1]*School of Mechanical Engineering and Electronic Information, China University of Geosciences (Wuhan), Wuhan 430074, China*
[2]*Wuhan National Laboratory for Optoelectronics, Wuhan 430074, China*
[3]*The Dodd-Walls Centre for Photonic and Quantum Technologies, Department of Physics, The University of Auckland, Auckland 1142, New Zealand*
[4]*School of Mathematics and Physics, China University of Geosciences (Wuhan), Wuhan 430074, China*
[5]*University of Limoges, UMR 7252, CNRS, XLIM Research Institute, F-87060 Limoges, France*

(Received 27 July 2020; revised 11 January 2021; accepted 15 January 2021; published 3 February 2021)

Dissipative Kerr solitons based on microresonators have wide applications from optical communications to optical ranging for the high-repetition rate and broad bandwidth. Restricted by the bending losses and dispersion control of the optical waveguide, it could be hard to further realize ultrahigh-repetetion rate reaching several terahertz by simply reducing the size of microresonators. Soliton crystals, which completely fill the microresonator with a series of equidistant temporal pulses, can be an effective approach to realize ultrahigh-repetition rate in the common cavity length. In this paper, we investigate the generation of soliton crystals in the presence of nonlinear mode coupling, which can induce a modulation on the background wave and modify the cavity dynamics. Under the condition of suitable wave vector mismatch and nonlinear-coupling-coefficient, high-deterministic perfect soliton crystals can be realized. Besides, the drifting behavior of the soliton crystals is demonstrated to be determined by the match between the wave vector mismatch and nonlinear coupling coefficient. Finally, we successfully observe the recrystallization of the perfect soliton crystals.

DOI: 10.1103/PhysRevA.103.023502

I. INTRODUCTION

Microresonator (MRR)-based dissipative Kerr solitons (DKSs), which are high-repetition-rate optical pulses circulating in the cavity, have wide applications for high-speed optical coherent communications [1], spectroscopy [2,3], microwave generation [4,5], astrocombs generation [6,7], optical ranging [8,9], etc. Different from the dissipative solitons generated in the mode-locked lasers [10], DKSs rely on the double balance between anomalous cavity dispersion and Kerr nonlinearity as well as parametric conversion of continuous-wave (CW) pump and cavity losses [11–13]. Because of many special properties such as chip-scale integration [14], broadband frequency domains (GHz [15] to THz [16]), and complementary metal-oxide semiconductor (CMOS) compatibility [17,18], the relative physical mechanisms and nonlinear dynamics of DKSs based on Kerr MRRs have been widely investigated to obtain high-quality microcombs [14,19]. As is known to all, the nonlinear dynamics of DKS are used to be divided into several characteristic states including spontaneous modulation instability (e.g., Turing patterns), spatiotemporal chaotic, breather soliton, and stable soliton states [20–22]. However, the spatiotemporal chaotic state often results in the stochastic number of DKS in the MRRs, which is usually more than one. The spectrum of multiple solitons shows many ditches due to the interference from the interacting DKSs [23,24]. Thus, different schemes for single soliton generation have been investigated to obtain a smooth spectrum for better applications [25–27].

Recently, a specific soliton state named soliton crystals (SCs) has been experimentally demonstrated in the SiN [28] and silica glass MRRs [29] as well as the silica whispering-gallery-mode (WGM) resonators [30]. According to their results, clearly discrete comb lines can be observed and the corresponding temporal pattern displays a series of equidistant DKSs, which fill the entire angular domain of the resonator. Thanks to the highly ordered soliton configuration and several primary comb lines distribution, high-repetition-rate ultrashort temporal pulses and n^2 enhanced comb power can be obtained through SCs formation, which can effectively avoid bending losses and dispersion management led by small MRR [31]. It should be noticed that related work [28] has demonstrated that avoided mode crossings (AMXs) generally existed in MRRs are able to induce the SCs formation. AMXs originated from the interaction of fundamental modes alter the localized MRR dispersion, which induces (quasi)homogeneous modulations on the CW pumping of the cavity [30,32]. Actually, the modulated wave can not only be induced by AMXs but also Kelly sidebands [33], birefringence [34], and nonlinear mode couplings including second [23] and third harmonic [24]. If we consider weak effects of Kelly sidebands and birefringence in the MRRs, nonlinear mode couplings could be of great potential to achieve the SCs formation. Some works on nonlinear mode coupling have been investigated including dark soliton formation [35],

*huangty@cug.edu.cn

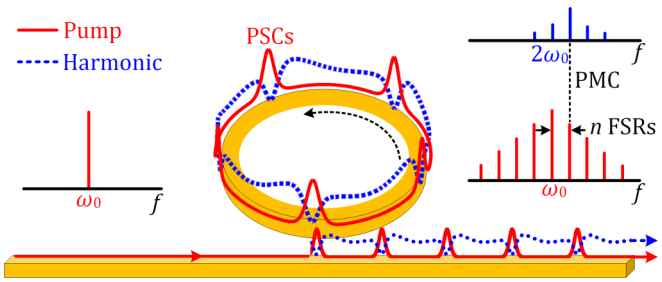

FIG. 1. Schematic diagram of nonlinear-mode-coupling-induced SCs formation in monolithic Kerr MRRs. The MRR is externally driven by a CW pump laser and the dimensions of the MRR satisfy the PMC between the fundamental and the harmonic waves.

soliton regulation [24], and deterministic single soliton formation [23]. Yet, to date, the dynamics of the SCs induced by nonlinear mode coupling remains unexplored.

In this paper, the SCs formation induced by nonlinear mode coupling is investigated in detail. We demonstrate the formation of perfect soliton crystals (PSCs) are tightly linked to nonlinear coupling coefficient and wave vector mismatch between fundamental and harmonic modes, which determine the conversion efficiency from pump to harmonic and phase matching condition (PMC), respectively. With appropriate choice of suitable wave vetor mismatch and nonlinear coupling coefficient, high deterministic PSCs containing specified numbers of solitons can be obtained. With further research, we find that the match between wave vector mismatch and nonlinear coupling coefficient play an important role for the generation of the SCs, while determining the drifting direction of the PSCs. We reveal the threshold of pump power, beyond which deterministic PSCs cannot be formed. In addition, we observe the SCs with different kinds of defects such as vacancy (Schottky defects) and superstructure [30]. In order to demonstrate the robustness of the PSCs generated by the nonlinear mode coupling process, we report the melting-recrystallization cycle of PCSs by accurately varying the cavity detuning.

II. THEORETICAL MODEL

To visually observe the PSCs formation based on nonlinear mode coupling, the process is depicted in Fig. 1. As can be seen, the CW pump from the bus waveguide is coupled into the cavity and then the PSCs at the fundamental wave and a series of optical pulses at the harmonic wave can be excited by scanning the pump wavelength over the cavity resonance. In the frequency domain, the adjacent comb lines of the fundamental and harmonic waves are spaced by n time free spectral ranges (FSRs) of the resonator, where n refers to the soliton number in PCSs.

Actually, the microcomb generation based on the residual second-order nonlinearity has been theoretically and experimentally demonstrated in SiN and AlN microcavities [23,35,36]. Although the SiN-based materials are inherently centrosymmetric, special manufacturing methods such as sputtering and stressing can be used for the enhancement of the second-order nonlinearity [37,38]. Here, we choose the fundamental-second-harmonic (FD-SH) mode coupling as the major example to investigate the dynamics induced by nonlinear mode coupling. The propagation of the fundamental and second-harmonic waves in the cavity can be described by the coupled mean-field Lugiato-Lefever equations (LLEs) [35]:

$$\frac{\partial E_1}{\partial z} = \left(-\alpha_1 - i\delta_1 - i\frac{k_1''}{2}\frac{\partial^2}{\partial \tau^2} + i\gamma_1|E_1|^2 i2\gamma_{12}|E_2|^2\right)E_1 + i\kappa E_2 E_1^* + \eta_1 E_{\text{in}}, \tag{1}$$

$$\frac{\partial E_2}{\partial z} = \left(-\alpha_2 - i\Delta k - i2\delta_1 - \Delta k'\frac{\partial}{\partial \tau} - i\frac{k_2''}{2}\frac{\partial^2}{\partial \tau^2} + i\gamma_2|E_2|^2 + i2\gamma_{21}|E_1|^2\right)E_2 + i\kappa^* E_1^2, \tag{2}$$

where $E_j (j = 1, 2)$ is the envelope of the electric field, 1 and 2 represent the fundamental and the second-harmonic waves, respectively; $|E_j|^2$ represents the power of the optical field; z is the propagation distance in the cavity; α_1 and α_2 are the total losses including the intrinsic and the coupling losses; $\delta_1 = \delta_0/L$, where L is the cavity length and δ_0 is round-trip phase detuning between the pump frequency ω_p and resonance frequency ω_0, defined as $\delta_0 = (\omega_0 - \omega_p)\tau_R$; $k_1'' = d^2k_p/d\omega^2|_\omega = \omega_p$, $k_2'' = d^2k_s/d\omega^2|_\omega = 2\omega_p$ are the group velocity dispersions (GVD), where k_p and k_s are wave vectors of the pump and second harmonic, respectively. $\Delta k' = dk_s/d\omega|_{2\omega_p} - dk_p/d\omega|_{\omega_p}$ is the group velocity mismatch; $\Delta k = 2k_p|_{\omega=\omega_p} - k_s|_{\omega=2\omega_p}$ is wave vector mismatch; γ_1, γ_2 are the nonlinear coefficients of self-phase modulation; γ_{12}, γ_{21} are the nonlinear coefficients of cross-phase modulation; κ is the second-order coupling coefficient, and $\eta_1 = \sqrt{\theta_1}/L$, where θ_1 is the power coupling coefficient between the bus waveguide and the microcavity at the pump wavelength.

III. RESULTS AND DISCUSSIONS

To demonstrate the effects of the fundamental-harmonic mode coupling, the Kerr MRR is assumed to sustain both fundamental mode and harmonic mode nearly satisfying the PMC. Then we choose the related physical parameters the same to Ref. [23], which are listed as follows: $\alpha_1 = 3.038\ \text{m}^{-1}$, $\alpha_3 = 6.07\ \text{m}^{-1}$, $k_1'' = -100\ \text{ps}^2/\text{km}$, $k_2'' = 200\ \text{ps}^2/\text{km}$, $\Delta k' = 7.61 \times 10^{-10}\ \text{s/m}$, $\gamma_1 = 0.8\ \text{W}^{-1}\text{m}^{-1}$, $\gamma_2 = 2.1\ \text{W}^{-1}\text{m}^{-1}$, $\gamma_{12} = 0.6\ \text{W}^{-1}\text{m}^{-1}$, $\gamma_{21} = 1.2\ \text{W}^{-1}\text{m}^{-1}$, $\kappa = 3\ \text{W}^{-1}\text{m}^{-1}$, $\eta_1 = 75.51\ \text{m}^{-1}$. Besides, to successfully obtain the PSCs, we set $\Delta k = -4.68 \times 10^3\ \text{m}^{-1}$ and $P_{\text{in}} = 22$ mW. The initial intracavity waveform is white Gaussian noise and the detuning scanning speed $(\Delta\delta_0)$ is 1×10^{-7} per round trip and the detuning is fixed when the PSCs state is established. In this condition, the value of Δk is estimated to satisfy the PMC at mode number $n = 5$ according to the following equations [23]:

$$\Delta\phi = \phi(2\omega_p + n\Delta\omega) - \phi(\omega_p) - \phi(\omega_p + n\Delta\omega) = \left(-\Delta k - 2\delta_1 - \Delta k' n\Delta\omega + \frac{k_2''}{2}(n\Delta\omega)^2 + \gamma_2\langle|E_2|^2\rangle + 2\gamma_{21}\langle|E_1|^2\rangle\right)L, \tag{3}$$

where $\phi(\omega_p)$ and $\phi(\omega_p + n\Delta\omega)$ are the round-trip phase at the pump modes, which are equal to zero for the SCs state. n

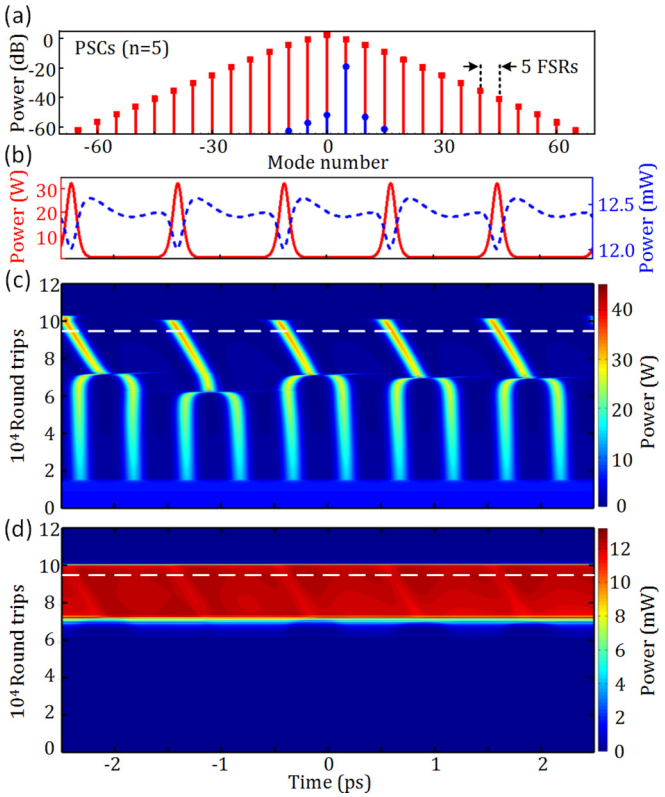

FIG. 2. (a) Spectra of fundamental (red vertical lines with squares) and harmonic (blue vertical lines with circles) waves in the PSCs state. (b) Temporal waveforms of fundamental (red solid line) and harmonic (blue dashed line) waves in the PSCs state. (c)–(d) Intracavity waveform evolutions of fundamental and second-harmonic waves, respectively.

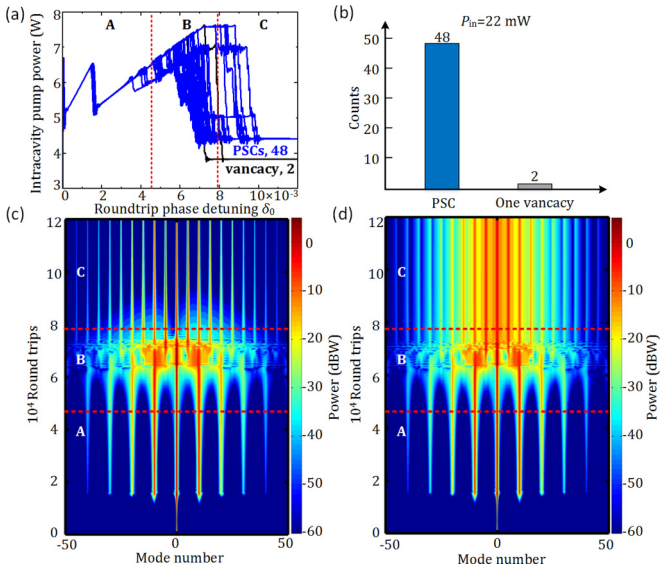

FIG. 3. (a) Intracavity power of the fundamental wave with respect to round-trip phase detuning δ_0, Blue lines: PSCs, black lines: SCs with one vacancy. (b) A statistical overview of the generated soliton states out of 50 scans with the same parameters in Fig. 2. (c)–(d) Two kinds of spectra evolutions of the fundamental wave for PSCs and SCs with one vacancy, respectively.

is the relative mode number with respect to the fundamental mode $\omega_p(n=0)$ and $\Delta\omega = 2\pi\mathrm{FSR}$. $\phi(2\omega_p + n\Delta\omega)$ is the round-trip phase of the second-harmonic wave. $\langle|E_1|^2\rangle$ and $\langle|E_2|^2\rangle$ represent the average power of the fundamental wave and second-harmonic wave, respectively.

Based on the preciously defined parameters, we performed numerical simulations by split-step Fourier method to solve Eqs. (1)–(2). As can be seen in Fig. 2(a), the spectrum of the fundamental wave is similar to the one induced by AMXs [28] and the adjacent comb line space equals five FSRs corresponding to the number of solitons ($n = 5$) in Fig. 2(b), which are the temporal waveforms at 9.5×10^4th round trip marked as white dashed lines in Figs. 2(c) and 2(d). The harmonic wave has the same comb line space and it exhibits dark pulselike temporal waveform. Compared to the combs in single soliton state, the PSCs have broader spectra and higher intensity. For the intracavity waveform evolution of fundamental wave shown in Fig. 2(c), partially adjacent solitons start to collide and merge into one after Turing state (6×10^4th round trip). With the power of harmonic wave increasing, shown in Fig. 2(d), the stronger interaction between fundamental and harmonic waves leads to more frequent soliton collisions till five solitons left (7×10^4th round trip). Finally, the PSCs and the dark pulselike waveform are left-drifting with the same velocity of 1.24×10^{-5} ps/round trip. Such phenomenon is similar to the case in the presence of AMXs. The mechanism of the process can be interpreted as localized dispersion alteration of the fundamental sideband mode due to the substantial photon exchange of sideband modes caused by the wave vector mismatch. Such effect leads to a small modulation on the CW background wave, whose total periods are equal to the sideband mode number. Then the modulation will arrange the solitons to lie on the peak of the background wave leading to the soliton collisions. Apart from the PSCs shown in Fig. 2, we can obtain other PSCs containing different number of solitons such as four solitons and six solitons corresponding to $\Delta k = -3.77 \times 10^3$ m^{-1} and $\Delta k = -5.64 \times 10^4$ m^{-1}, respectively.

Considering that the SCs is presumably to be generated in the cavity with anomalous dispersion, we investigate the determinacy of the PSCs formation induced by FD-SH mode coupling. Figure 3(b) shows the statistical results out of 50 scans with the same parameters in Fig. 2. Forty-eight times for the PSCs and two times for the SCs with one vacancy indicate deterministic PSCs formation. All intracavity power traces of the 50 scans are shown in Fig. 3(a), which are 48 blue lines for the PSCs and two black lines for the SCs with one vacancy, respectively. The red dashed lines divide the power traces into three parts marked from A to C indicating Turing patterns, chaotic state, and SCs state, respectively. The spectrum evolutions shown in Figs. 3(c) and 3(d) corresponds to the PSCs and the SCs with one vacancy chosen from the 50 scans, which are also divided by the red dashed lines exactly corresponding to the specific states in Fig. 3(a).

We would like to notice that $\Delta k = -4.68 \times 10^3$ m^{-1} and $\kappa = 3$ W^{-1}m^{-1} in Fig. 2 are exemplary parameters used in the numerical simulations for PSCs formation. Actually, the phase mismatch can be within the range from -4.73×10^3 m^{-1} to -4.63×10^3 m^{-1} according to our simulations. Besides, we

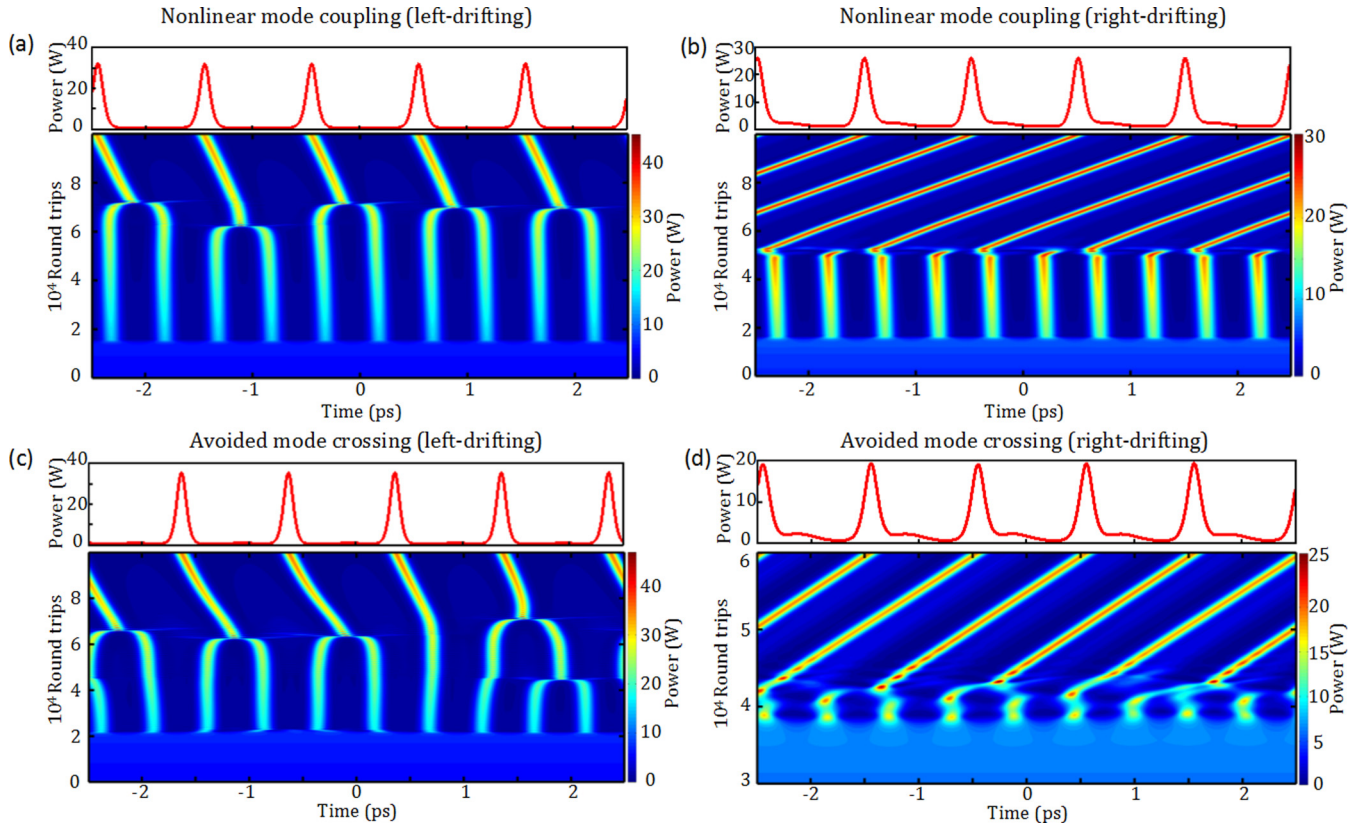

FIG. 4. (a)–(b) Intracavity waveform evolutions of fundamental wave induced by FD-SH mode coupling when $\Delta k = -4.68 \times 10^3$ m^{-1}, $\kappa = 3$ W^{-1}m^{-1}, and $\Delta k = -4.603 \times 10^3$ m^{-1}, $\kappa = 3.6$ W^{-1}m^{-1}, respectively. (c)–(d) Intracavity waveform evolutions induced by AMXs with $\Delta = -12.7$ MHz and 133.7 MHz, respectively.

can also obtain PSCs with the same number of solitons ($n = 5$) when $\Delta\kappa = -4.603 \times 10^3$ m^{-1} and $\kappa = 3.6$ W^{-1}m^{-1} with other parameters unchanged, as shown in Fig. 4(b). In the FD-SH coupling case, the coupling strength is determined by both Δk and κ, which is different from the linear coupling of AMXs. With larger absolute value of Δk, the nonlinear coupling coefficient κ should be larger to ensure sufficient photon exchange between fundamental and second-harmonic waves. Thus the match between Δk and κ finally contributes to the deterministic PSCs formation. Compared to the left-drifting PSCs shown in Fig. 4(a), the PSCs shown in Fig. 4(b) are right drifting. To understand the drifting direction of PSCs induced by FD-SH coupling, we compare the nonlinear induced PSCs to the one induced by AMXs, which also lead to localized dispersion alteration. In the condition of AMX, we ignore the harmonic wave ($E_2 = 0, \kappa = 0$) and Eqs. (1)–(2) can be simplified to a single LLE [39]. AMXs is included by introducing an additional detuning variation per round trip (Δ) for a certain mode with mode number n defined as $\delta_n = (\omega_n - \omega_p)\tau_R = [(\omega_0 + 2\pi\ \mathrm{FSR}n + \Delta) - \omega_p]\tau_R$. Keeping all parameters of fundamental wave (E_1) constant, we add an additional detuning to the mode $n = 5$. As can be seen, PSCs shown in Fig. 4(c) with $\Delta/2\pi = -12.7$ MHz is left drifting and PSCs shown in Fig. 4(d) with $\Delta/2\pi = 133.7$ MHz is right drifting. Thus the drifting direction is tightly linked to the sign of Δ. Based on the results of AMXs, we can understand the drifting direction induced by FD-SH coupling in this way: the localized dispersion alteration determined by the match between Δk and κ will introduce a negative/positive detuning variation to the sideband mode of the fundamental wave, which acts as a perturbation to excite the formation of drifting PSCs.

To gain more insights into the drifting direction of the PSCs, we run the following simulations to figure out the cooperation between the wave vector mismatch Δk and the second-order coupling coefficient κ, and the relevant results are shown in Fig. 5. With 0.1W^{-1}m^{-1} variation step of κ, we obtain the complete suitable range of Δk for PSCs formation. The blue and red areas in Fig. 5(a) indicate the left-drifting and right-drifting PSCs, respectively. The PSCs with other number of solitons, SCs with vacancy and multiple solitons state are classified into the cream areas. As can be seen, the range of wave vector mismatch Δk increases with increasing the coefficient κ and the drifting direction always keeps to the left corresponding to the blue area in Fig. 5(a). When κ is more than 3.1 W^{-1}m^{-1}, beside the blue area, the range of Δk corresponding to the red area increases together with κ. The results in Figs. 4(a)–4(b) exactly correspond to the black circle and triangle, which are, respectively, marked as A and C. For $\kappa > 3.1$ W^{-1}m^{-1}, there is an intersection between the blue and the red areas indicating that both left-drifting and right-drifting PSCs can be obtained with suitable wave vector mismatch. Figures 5(b)–5(c) correspond to the black circle and triangle marked as B and C in Fig. 5(a), respectively. Comparing the two temporal evolutions, we can see that the right-drifting PSCs display a faster-drifting velocity.

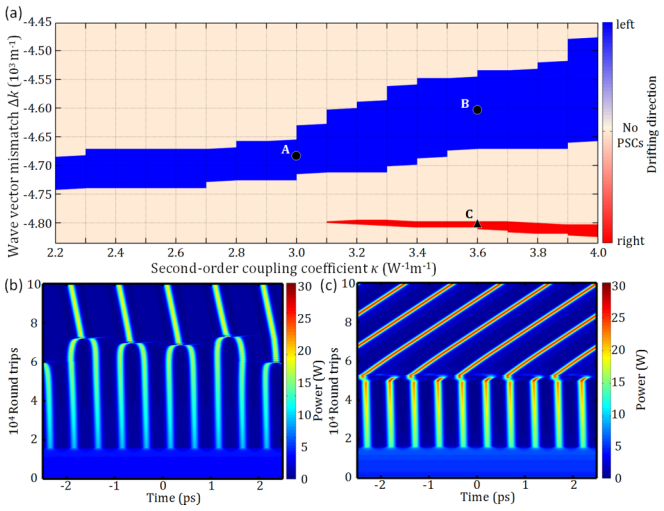

FIG. 5. (a) Drifting direction depending on the range of the wave vector mismatch Δk and the second-order coupling coefficient κ. (b)–(c) Temporal evolutions of the left-drifting and right-drifting PSCs corresponding to the black circle and triangle marked as B and C, respectively.

Apart from the wave vector mismatch Δk and coupling coefficient κ, the pump power has a significant impact on the PSCs formation. When increasing the pump power P_{in} to 32 mW, the statistical results shown in Fig. 6(a) indicate that the determinacy of the PSCs decrease a lot compared to that in Fig. 3. Further increasing P_{in} to 50 mW, the generation of the SCs with vacancies is dominated as is shown in Fig. 6(b). Thus the threshold of the pump power P_{in} is estimated to be 32 mW based on our simulations. Besides, we investigate the dynamics of the SCs with one vacancy when $P_{\text{in}} = 50$ mW, the temporal waveform evolutions of fundamental and second-harmonic waves are shown in Figs. 6(e)–6(f). Compared to the results shown in Figs. 2(c)–2(d), the intracavtiy field of the fundamental wave with higher pump power transforms into the chaotic state after the Turing pattern, which makes the evolution process become erratic. By gradually scanning the round-trip phase detuning, the SCs with a vacancy finally appear and the harmonic wave also shows a corresponding vacancy [Fig. 6(d)], which are different from the waveforms shown in Fig. 2(b). References [29,30] have reported that the SCs with defects induced by AMXs are sensitive to the pump power, which will intensifies the fluctuations in the chaotic state thus changing the initial conditions. For nonlinear-mode-coupling-induced SCs formation, a larger pump power will also lead to a more complex interaction between solitons [cf. Fig. 6(e)]. Besides, we find that a larger wave vector mismatch will also lead to the SCs with defects. Figure 7 shows two kinds of SCs exhibiting one vacancy and superstructure, which are under the conditions: $P_{\text{in}} = 22$ mW, $\Delta k = -4.74 \times 10^3$ m^{-1} and $P_{\text{in}} = 22$ mW, $\Delta k = -1.03 \times 10^4$ m^{-1}, respectively. It should be pointed out that the time windows of Figs. 7(a) and 7(c) correspond to one round trip of the resonator. From this point of view, Fig. 2(c) demonstrated the full process of crystallization of cavity solitons, which fill the full angular domain of the resonator. Figure 7(b) illustrates the characteristic saw-teeth intensity profiles and palmlike

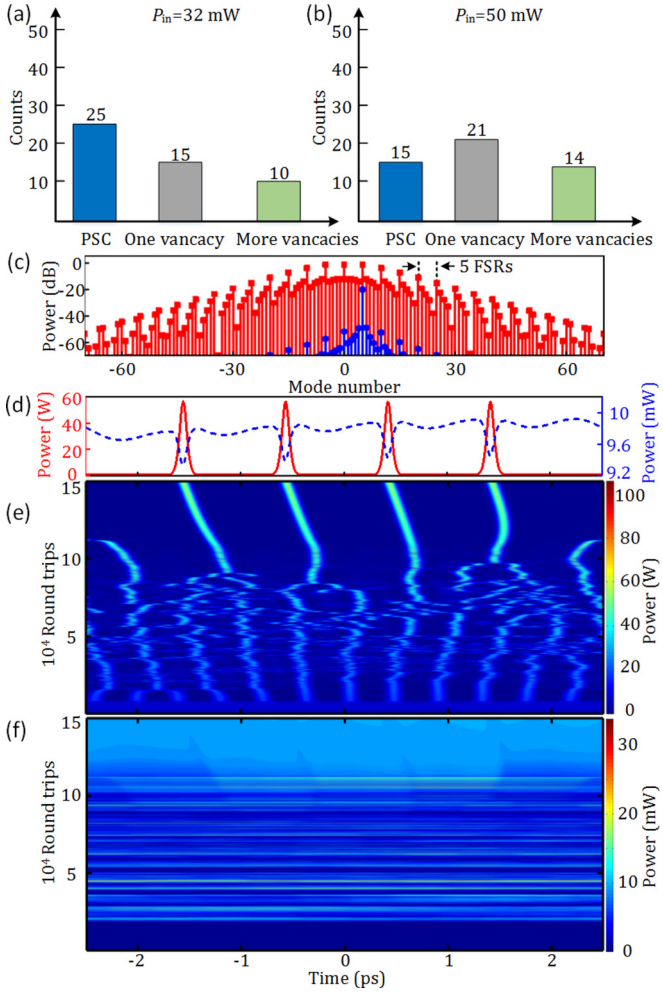

FIG. 6. (a)–(b) The statistical overviews of the generated soliton states out of 50 scans when $P_{\text{in}} = 32$ mW and $P_{\text{in}} = 50$ mW, respectively. The characteristic generation of SCs with on vacancy when $P_{\text{in}} = 50$ mW: (c) Spectra of the fundamental (red vertical lines with squares) and the harmonic (blue vertical lines with circles) waves, (d) Temporal waveforms of the fundamental (red solid line) and the harmonic (blue dashed line) waves in SCs state. (e)–(f) Intracavity waveforms evolution of fundamental and second-harmonic waves, respectively.

spectrum of soliton crystals in MRRs [29]. And Fig. 7(d) describes a characteristic scalloped spectrum, which with specific FSR has recently been proved to have high performance in ultradense optical data transmission [40].

Based on the linearly forward tuning, the PSCs induced by the nonlinear mode coupling has been demonstrated to be deterministic. Moreover, the robustness can be another important parameter for the PSCs. The phenomenon known as recrystallization of the PSCs state has theoretically and experimentally been demonstrated in the PSCs formation induced by AMXs [28]. Here, we utilize this process through backward tuning to the chaotic state and forward tuning back to the PSCs again to show the robustness, the temporal evolution of which is shown in Fig. 8(a). We first increase the pump power of the PSCs shown in Fig. 2 to 30 mW to introduce a more complex interaction between the solitons during the chaotic state. Then the initial stable PSCs with clearly discrete

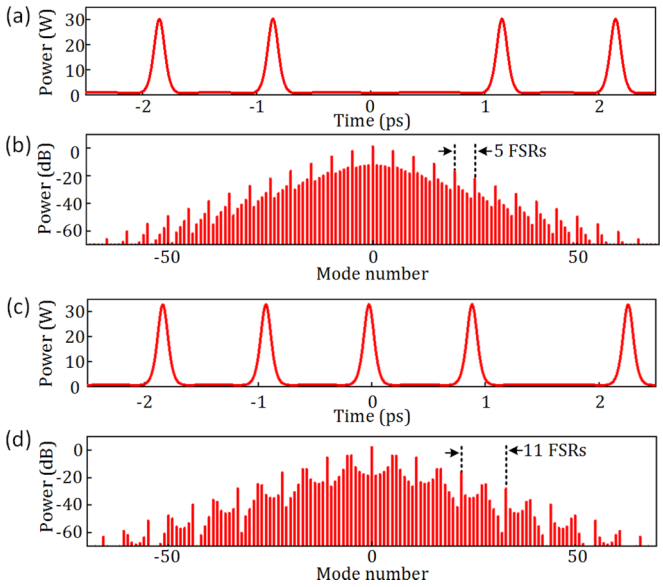

FIG. 7. Vacancy: (a) Temporal waveforms, (b) spectrum. Superstructure: (c) Temporal waveforms, (d) spectrum.

comb lines shown in Fig. 8(e) is obtained. With the backward tuning to the chaotic state, the additional comb lines begin to appear as is shown in Fig. 8(d) and gradually changes to a disordered spectrum shown in Fig. 8(c), which are also termed "PSCs melting" in Ref. [28]. After that, the forward tuning brings the intracavity waveforms back to the initial stable PSCs state shown in Fig. 8(b) indicating the success of the soliton recrystallization.

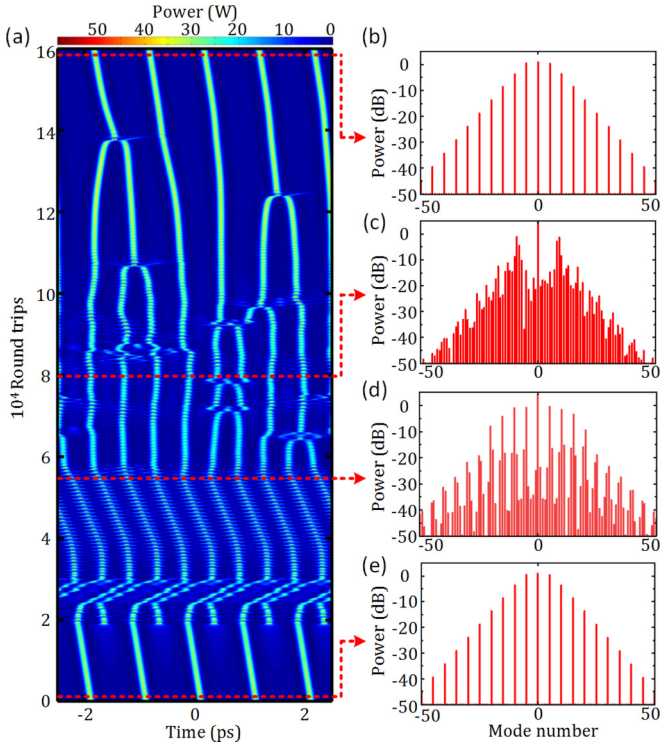

FIG. 8. (a) Temporal evolution of the PSCs melting and recrystallization through the backward tuning to the chaotic state and forward tuning back to the initial PSCs state. (b)–(e) The spectra at different tuning stages corresponding to the specific round trips in (a).

IV. DISCUSSION AND CONCLUSION

The above statistic analysis and the melting-recrystallization cycle of the PSCs state have not only strongly proved its robustness, but also confirmed the high repeatability for the generation. Compared to the scheme based on AMXs [28–30], the proposed one in this paper is able to generate two combs at both fundamental and harmonic wavelength regimes. More importantly, it provides another promising approach to obtain the frequency comb at shorter wavelength range by overcoming the limits of strong normal dispersion of the common photonics materials such as SiN and silica [41,42]. It is worth mentioning that we have mainly discussed the contributions of second harmonics. However, we would like to emphasize that other nonlinear coupling such as the third-harmonic generation (THG) will have similar effects. Previous work has proved that third harmonic is able to introduce a modulation on the background wave to arrange the temporal positions of the solitons in the MRRs. In fact, our additional numerical simulations have revealed that fundamental-third-harmonic (FD-TH)-induced crystallization of cavity solitons can also occur in the MMRs. It means that the generation of the SCs via the mode coupling between fundamental mode and higher-order harmonics are universal. However, the waveguide structures that fulfill the requirements of FD-TH-based nonlinear coupling still need to be developed. From this point of view, it removes many restrictions for the materials and geometrical design of MMRs.

In summary, we theoretically and numerically investigate the SCs formation induced by nonlinear mode coupling. With suitable wave vector mismatch and coupling coefficient, a deterministic PSCs can be obtained by simply sweeping the pump wavelength. We also find the drifting direction of the PSCs are tightly related to the match between the wave vector mismatch and the nonlinear coupling coefficient, which will introduce different detuning variation to a certain sideband mode. Besides, there is a threshold of pump power for the generation of the SCs, which is similar to that in the presence of AMXs. The nonlinear-coupling-induced soliton generation can be realized in the presence of either SHG or THG. This work can be a complementary part of the cavity soliton dynamics and provide a potential approach for high-repetition-rate pulse and dual-band comb generation.

ACKNOWLEDGMENTS

We acknowledge the support from the Open Project Program of Wuhan National Laboratory for Optoelectronics (Grant No. 2019WNLOKF005); the Natural Science Foundation of Hubei Province (Grant No. 2019CFB598); Wuhan Science and Technology Bureau (Grant No. 2018010401011297); the National Natural Science Foundation of China (Grant No. 61605179); the Fundamental Research Funds for the Central Universities, China University of Geosciences (Wuhan) (Grant No. 1910491B06, ZL201917, G1320311998).

[1] P. Marin-Palomo, J. N. Kemal, M. Karpov, A. Kordts, J. Pfeifle, M. H. P. Pfeiffer, P. Trocha, S. Wolf, V. Brasch, M. H. Anderson *et al.*, Microresonator-based solitons for massively parallel coherent optical communications, Nature (London) **546**, 274 (2017).

[2] M. G. Suh, Q. F. Yang, K. Y. Yang, X. Yi, and K. J. Vahala, Microresonator soliton dual-comb spectroscopy, Science **354**, 600 (2016).

[3] A. Dutt, C. Joshi, X. Ji, J. Cardenas, Y. Okawachi, K. Luke, A. L. Gaeta, and M. Lipson, On-chip dual-comb source for spectroscopy, Sci. Adv. **4**, e1701858 (2018).

[4] S. Diallo and Y. K. Chembo, Optimization of primary Kerr optical frequency combs for tunable microwave generation, Opt. Lett. **42**, 3522 (2017).

[5] X. Xue, Y. Xuan, H.-J. Kim, J. Wang, D. E. Leaird, M. Qi, and A. M. Weiner, Programmable single-bandpass photonic RF filter based on Kerr comb from a microring, J. Lightwave Technol. **32**, 20 (2014).

[6] E. Obrzud, M. Rainer, A. Harutyunyan, M. H. Anderson, J. Q. Liu, M. Geiselmann, B. Chazelas, S. Kundermann, S. Lecomte, M. Cecconi *et al.*, A microphotonic astrocomb, Nat. Photon. **13**, 31 (2019).

[7] M.-G. Suh, X. Yi, Y.-H. Lai, S. Leifer, I. S. Grudinin, G. Vasisht, E. C. Martin, M. P. Fitzgerald, G. Doppmann, J. Wang, D. Mawet, S. B. Papp, S. A. Diddams, C. Beichman, and K. Vahala, Searching for exoplanets using a microresonator astrocomb, Nature Photon. **13**, 25 (2019).

[8] P. Trocha, M. Karpov, D. Ganin, M. H. P. Pfeiffer, A. Kordts, S. Wolf, J. Krockenberger, P. Marin-Palomo, C. Weimann, S. Randel, W. Freude, T. J. Kippenberg, and C. Koos, Ultrafast optical ranging using microresonator soliton frequency combs, Science **359**, 887 (2018).

[9] M.-G. Suh and K. J. Vahala, Soliton microcomb range measurement, Science **359**, 884 (2018).

[10] P. Grelu, and N. Akhmediev, Dissipative solitons for mode-locked lasers, Nature Photon. **6**, 84 (2012).

[11] M. Haelterman, S. Trillo, and S. Wabnitz, Dissipative modulation instability in a nonlinear dispersive ring cavity, Opt. Commun. **91**, 401 (1992).

[12] T. J. Kippenberg, A. L. Gaeta, M. Lipson, and M. L. Gorodetsky, Dissipative Kerr solitons in optical microresonators, Science **361**, eaan8083 (2018).

[13] T. Herr, V. Brasch, J. D. Jost, C. Y. Wang, N. M. Kondratiev, M. L. Gorodetsky, and T. J. Kippenberg, Temporal solitons in optical microresonators, Nat. Photon. **8**, 145 (2014).

[14] B. Stern, X. C. Ji, Y. Okawachi, A. L. Gaeta, and M. Lipson, Battery-operated integrated frequency comb generator, Nature (London) **562**, 401 (2018).

[15] X. Yi, Q.-F. Yang, K. Y. Yang, M.-G. Suh, and K. Vahala, Soliton frequency comb at microwave rates in a high-Q silica microresonator, Optica **2**, 1078 (2015).

[16] T. E. Drake, T. C. Briles, Q. Li, D. A. Westly, R. Ilic, J. R. Stone, K. Srinivasan, S. A. Diddams, and S. B. Papp, An octave-bandwidth kerr optical frequency comb on a silicon chip, in *Conference on Lasers and Electro-Optics*, OSA Technical Digest (Optical Society of America, 2016), paper STu3Q.4.

[17] V. Brasch, M. Geiselmann, T. Herr, G. Lihachev, M. H. P. Pfeiffer, M. L. Gorodetsky, and T. J. Kippenberg, Photonic chip–based optical frequency comb using soliton Cherenkov radiation, Science **351**, 357 (2016).

[18] A. S. Raja, A. S. Voloshin, H. R. Guo, S. E. Agafonova, J. Q. Liu, A. S. Gorodnitskiy, M. Karpov, N. G. Pavlov, E. Lucas, and R. R. Galiev, Electrically pumped photonic integrated soliton microcomb, Nat. Commun. **10**, 680 (2019).

[19] B. Yao, S. Huang, Y. Liu, A. K. Vinod, C. Choi, M. Hoff, Y. Li, M. Yu, Z. Feng, D. L. Kwong *et al.*, Gate-tunable frequency combs in graphene–nitride microresonators, Nature (London) **558**, 410 (2018).

[20] S. Coen and M. Erkintalo, Universal scaling laws of Kerr frequency combs, Opt. Lett. **38**, 1790 (2013).

[21] C. Godey, I. V. Balakireva, A. Coillet, and Y. K. Chembo, Stability analysis of the spatiotemporal Lugiato-Lefever model for Kerr optical frequency combs in the anomalous and normal dispersion regimes, Phys. Rev. A **89**, 063814 (2014).

[22] P. Parra-Rivas, D. Gomila, M. Matías, S. Coen, and L. Gelens, Dynamics of localized and patterned structures in the Lugiato-Lefever equation determine the stability and shape of optical frequency combs, Phys. Rev. A **89**, 043813 (2014).

[23] X. Xue, X. Zheng, and B. Zhou, Soliton regulation in microcavities induced by fundamental–second-harmonic mode coupling, Photonics Res. **6**, 948 (2018).

[24] J. Pan, Z. Cheng, T. Huang, C. Song, P. P. Shum, and G. Brambilla, Fundamental and third harmonic mode coupling induced single soliton generation in Kerr microresonators, J. Lightwave Technol. **37**, 21 (2019).

[25] H. Guo, M. Karpov, E. Lucas, A. Kordts, M. H. P. Pfeiffer, V. Brasch, G. Lihachev, V. E. Lobanov, M. L. Gorodetsky, and T. J. Kippenberg, Universal dynamics and deterministic switching of dissipative Kerr solitons in optical microresonators, Nat. Phys. **13**, 94 (2017).

[26] X. Yi, Q.-F. Yang, K. Y. Yang, and K. Vahala, Active capture and stabilization of temporal solitons in microresonators, Opt. Lett. **41**, 2037 (2016).

[27] H. Taheri, A. A. Eftekhar, K. Wiesenfeld, and A. Adibi, Soliton formation in whispering-gallery-mode resonators via input phase modulation, IEEE Photon. J. **7**, 2200309 (2015).

[28] M. Korpov, M. H. P. Pfeiffer, H. Guo, W. Weng, J. Liu, and T. J. Kippenberg, Dynamics of soliton crystals in optical microresonators, Nat. Phys. **15**, 1071 (2019).

[29] W. Wang, Z. Lu, W. Zhang, S. T. Chu, B. E. Litte, L. Wang, X. Xie, M. Liu, Q. Yang, L. Wang, J. Zhao, G. Wang, Q. Sun, Y. Liu, Y. Wang, and W. Zhao, Robust soliton crystals in a thermally controlled microresonator, Opt. Lett. **43**, 2002 (2018).

[30] D. C. Cole, E. S. Lamb, P. Del'Haye, S. A. Diddams, and S. B. Papp, Soliton crystals in Kerr resonators, Nat. Photon. **11**, 671 (2017).

[31] Y. Xu, Y. Lin, A. Nielsen, I. Hendry, S. Coen, M. Erkintalo, H. Ma, and S. G. Murdoch, Harmonic and rational harmonic driving of microresonator soliton frequency combs, Optica **7**, 940 (2020).

[32] C. Bao, Y. Xuan, D. E. Leaird, S. Wabnitz, M. Qi, and A. M. Weiner, Spatial mode-interaction induced single soliton generation in microresonators, Optica **4**, 1011 (2017).

[33] A. U. Nielsen, B. Garbin, S. Coen, S. G. Murdoch, and M. Erkintalo, Invited article: Emission of intense resonant radiation by dispersion-managed Kerr cavity solitons, APL Photonics **3**, 120804 (2018).

[34] A. U. Nielsen, B. Garbin, S. Coen, S. G. Murdoch, and M. Erkintalo, Coexistence and Interactions between Nonlinear States with Different Polarizations in a Monochromatically

Driven Passive Kerr Resonator, Phys. Rev. Lett. **123**, 013902 (2019).

[35] X. Xue, F. Leo, Y. Xuan, J. A. Jaramillo-Villegas, P. H. Wang, D. E. Leaird, M. Erkintalo, M. Qi, and A. M. Weiner, Second-harmonic-assisted four-wave mixing in chip-based microresonator frequency comb generation, Light Sci. Appl. **6**, e16253 (2017).

[36] X. Guo, C.-L. Zou, H. Jung, Z. Gong, A. Bruch, L. Jiang, and H. X. Tang, Efficient Visible Frequency Comb Generation via Cherenkov Radiation from a Kerr Microcomb, Phys. Rev. Appl. **10**, 014012 (2018).

[37] A. Kitao, K. Imakita, I. Kawamura, and M. Fujii, An investigation into second harmonic generation by si-rich SiNx thin films deposited by RF sputtering over a wide range of si concentrations, J. Phys. D: Appl. Phys. **47**, 215101 (2014).

[38] M. Cazzanelli, F. Bianco, E. Borga, G. Pucker, M. Ghulinyan, E. Degoli, E. Luppi, V. Véniard, S. Ossicini, D. Modotto, S. Wabnitz, R. Pierobon, and L. Pavesi, Second-harmonic generation in silicon waveguides strained by silicon nitride, Nat. Mater. **11**, 148 (2012).

[39] S. Coen, H. G. Randle, T. Sylvestre, and M. Erkintalo, Modeling of octave-spanning Kerr frequency combs using a generalized mean-field Lugiato–Lefever model, Opt. Lett. **38**, 37 (2013).

[40] B. Corcoran, M. Tan, X. Xu, A. Boes, J. Wu, T. G. Nguyen, S. T. Chu, B. E. Little, R. Morandotti, A. Mitchell, and D. J. Moss, Ultra-dense optical data transmission over standard fibre with a single chip source, Nat. Commun. **11**, 2568 (2020).

[41] S. Miller, K. Luke, Y. Okawachi, J. Cardenas, A. L. Gaeta, and M. Lipson, On-chip frequency comb generation at visible wavelengths via simultaneous second- and third-order optical nonlinearities, Opt. Express **22**, 26517 (2014).

[42] H. Zhao, B. Kuyken, S. Clemmen, F. Leo, A. Subramanian, A. Dhakal, P. Helin, S. Severi, E. Brainis, G. Roelkens, and R. Baets, Visible-to-near-infrared octave spanning supercontinuum generation in a silicon nitride waveguide, Opt. Lett. **40**, 2177 (2015).